



## Research Article

# Multifunctional hosts of Zinc sulfide coated carbon nanotubes for lithium sulfur batteries

Honghong Liu<sup>1,2</sup> · Tiju Thomas<sup>3</sup> · Rongrong Li<sup>1,2</sup> · Hangjia Shen<sup>1,2</sup>  · Jiacheng Wang<sup>1,2,4</sup> · Minghui Yang<sup>1,2</sup>

Received: 31 March 2020 / Accepted: 27 May 2020 / Published online: 2 June 2020

© Springer Nature Switzerland AG 2020

## Abstract

Lithium sulfur (Li–S) batteries are next general energy storage systems due to their high theoretical energy density, low cost and environmental friendly. Herein, we develop a composite polysulfide mediator based on carbon nanotubes enwrapped by zinc sulfide (CNTs@ZnS) nanoparticles as multifunctional host materials for sulfur cathode. The ZnS nanoparticles is uniformed coating on the outside layer of functionalized carbon nanotubes. The unique structure of CNTs@ZnS ensure the chemical adsorption on ZnS and fast electron transfer from ZnS to carbonnanotubes. The presence of ZnS efficiently alleviates the shuttle effect of soluble lithium polysulfide intermediates and hence offers a mean to further enhancing the reaction activity via sulfophilic property of ZnS and catalytically accelerate the conversion of polysulfides to insoluble Li<sub>2</sub>S. The high conductivity of carbon nanotubes results in rapid electron transfer. The CNTs@ZnS cathode offers an excellent specific capacity of ~ 1003 mAh g<sup>-1</sup> after 100 cycles at 0.2C. Furthermore significant cycling performance at 0.2C with 3.1 mg cm<sup>-2</sup> sulfur loading for 500 cycles is observed with 0.05% capacitance decay per cycle. The results provide insights to develop high-performance Li–S batteries based on multifunctional host materials.

**Keywords** Zinc sulfide · Carbon nanotubes · Lithium sulfur batteries · Chemical adsorption · Enhanced reaction activities

## 1 Introduction

With the industrial and economic growth, energy plays a critical role in present and future. The needs of energy are evidently growing and there is an evident need for reorganization of the economy around renewable energy sources. This in turn implies the need for large scale rechargeable energy storage devices [1–3]. In order to improve the efficiency of electric power utilization, stable and sustainable energy storage systems with low

cost and eco-friendly are essential [4, 5]. Lithium sulfur (Li–S) batteries are emerging as a promising new generation of energy storage devices for electric vehicles and portable energy devices [6–8]. It is known that the Li–S batteries possess high theoretical specific capacity of 1675 mAh g<sup>-1</sup> and energy density of 2600 Wh kg<sup>-1</sup>, which is five times higher than that of commercially available lithium ion batteries [8–10]. Meanwhile, the low cost and abundance of sulfur make it possible for large scale energy storage [11, 12]. However, there are

**Electronic supplementary material** The online version of this article (<https://doi.org/10.1007/s42452-020-2964-0>) contains supplementary material, which is available to authorized users.

✉ Hangjia Shen, shenhj@nimte.ac.cn; ✉ Jiacheng Wang, jiacheng.wang@mail.sic.ac.cn; ✉ Minghui Yang, myang@nimte.ac.cn | <sup>1</sup>Solid State functional Materials Research Laboratory, Ningbo Institute of Materials Technology and Engineering, Chinese Academy of Sciences, Ningbo 315201, China. <sup>2</sup>Center of Materials Science and Optoelectronics Engineering, University of Chinese Academy of Sciences, Beijing 100049, China. <sup>3</sup>Department of Metallurgical and Materials Engineering, Indian Institute of Technology Madras, Adyar, Chennai, Tamil Nadu 600036, India. <sup>4</sup>The State Key Laboratory of High Performance Ceramics and Superfine Microstructure, Shanghai Institute of Ceramics, Chinese Academy of Sciences, 1295 Dingxi Road, Shanghai 200050, China.



SN Applied Sciences (2020) 2:1156 | <https://doi.org/10.1007/s42452-020-2964-0>

still significant obstacles for the practical application of Li–S batteries [13–15].

The major concern revolves the low utilization of sulfur and the slow kinetics of the associated electrochemical redox reactions because the electrical insulation of sulfur and  $\text{Li}_2\text{S}$  limits electrons and lithium ions transportation in the electrode [16, 17]. Meanwhile, the intermediate polysulfides ( $\text{Li}_2\text{S}_x$ ,  $2 < x < 8$ ) are soluble in the organic electrolytes and they shuttle between anode and cathode. The dissolved polysulfides directly react with lithium ions and electrons on the lithium anode surface (shuttle effect); which results in low Coulombic efficiency, fast capacity decay and poor cycle stability [7, 18]. Finally, the large volume expansion of the sulfur particles leads to the breakage of cathode's structure and rapid capacity fading [19].

Currently, extensive research efforts have been devoted to enhance the electrochemical performance of cathode materials [10, 20]. Various carbon-based materials including carbon nanofiber [21], carbon nanotube and graphene have been designed as effective cathode hosts for sulfur loading. These carbon based materials can restrain the shuttle effect by physical confinement and improve the conductivity of the cathodes [22]. Unfortunately, the non-polar carbon-based materials used as cathodes, exhibit weak interaction with polar lithium polysulfide intermediates (LiPSs). This in fact results in the degradation of cycling stability and rate capability. On the other hand, polar inorganic metal-based materials can efficiently prevent the loss of active sulfur materials and hence chemically anchor LiPSs for advanced Li–S batteries. Recently, metal oxides such as  $\text{MoO}_2$  [23],  $\text{TiO}_2$  [24, 25],  $\text{SnO}_2$  [26] and  $\text{MnO}_2$  [27, 28] have been explored as chemical trappers to bind LiPSs through polar chemical interaction in the cathodes. However, due to the poor conductivity of metal oxides, the fabricated Li–S batteries exhibit poor rate performance and low sulfur utilization. Furthermore, the sluggish reaction kinetics make the LiPSs assemble on the host surface and cause the adsorption of LiPSs decreased. For above reasons, an ideal sulfur host material should have high conductivity to insure the sufficient utilization of sulfur and should also have strong electrocatalytic activity to promote the conversion of LiPSs. To achieve this, metal sulfides (e.g.  $\text{Co}_9\text{S}_8$ ,  $\text{MoS}_2$ ,  $\text{WS}_2$ ,  $\text{SnS}_2$ , etc.) have been investigated as cathode materials for Li–S batteries. This is because of the strong sulfiphilic property of metal sulfides to sulfur-containing species [29, 30]. Furthermore, the metal sulfides can act as an activation catalyst to promote the oxidation of  $\text{Li}_2\text{S}$ , as indicated by Cui et al. [8]. As typical metal sulfides, zinc sulfide (ZnS) possesses the strong sulfiphilic property to LiPSs. Moreover, the polar feature of ZnS is also beneficial to adsorption and catalytic conversion of polar LiPSs.

Herein, zinc sulfide (ZnS) coated carbon nanotubes ( $\text{CNTs@ZnS}$ ) are synthesized as sulfur host with strong chemical adsorption and electrocatalytic activity towards LiPSs conversion for high performance Li–S batteries. The  $\text{CNTs@ZnS}$  composite is prepared using simple self-assembly of ZnS and CNTs. It is then thermally treated under argon. The product is composed of zinc sulfide nanoparticles, which assemble on carbon nanotubes. The core of carbon nanotubes can enhance the conductivity for electrons/ions transfer and provide physical entrapment of LiPSs. The ZnS acts as a sulfiphilic host that promotes the LiPSs redox process and improves the chemical adsorption to effectively trap the polysulfides. With the advantage of the synergetic effect between CNTs and ZnS, the sulfur loaded  $\text{CNTs@ZnS}$  cathode has a large capacity of 1003 mAh  $\text{g}^{-1}$  after 100 cycles at 0.2C. And the long cycle life with low capacity fading of 0.05% per cycle over 500 cycles at 0.2C with 3.1 mg  $\text{cm}^{-2}$  sulfur loading is observed in the Li–S batteries.

## 2 Experimental

### 2.1 Materials synthesis

Synthesis of carbon nanotubes (CNTs). A facile wet chemical method was employed to synthesize the carbon nanotubes (CNTs). In a typical experiment, 98 mg (0.3 mmol) of methyl orange powders (98%, Tokoyo Chemical) were dissolved in 60 mL deionized water under continuously stirring. Then 0.49 g (3 mmol) of anhydrous  $\text{FeCl}_3$  powder was added into the above solution and a flocculent precipitate was formed immediately. 210  $\mu\text{L}$  of pyrrole monomer (99%, Admas Reagent) was mixed in the solution and kept at 25 °C for 24 h. The black polypyrrole nanotubes were collected and washed with deionized water and ethanol several times until the filtrate turned colorless and neutral. The produced PPy-NTs were finally freeze-dried for 24 h. Then, 100 mg of the as-prepared PPy-NTs was placed in a quartz tube furnace and then heated under Ar environment from room temperature to 800 °C at a rate of 10 °C  $\text{min}^{-1}$  and kept for 3 h. After the furnace was cooled down to room temperature, the black CNTs powder was obtained.

Synthesis of  $\text{CNTs@ZnS}$ . The resultant  $\text{CNTs@ZnS}$  was obtained by hydrothermal method. 20 mg of CNTs was dispersed in 60 mL of ethylene glycol under stirring. Then, 0.46 g (1.3 mmol) of cetyltrimethylammonium bromide (CTAB, Aladdin) powder, 0.37 g (1.2 mmol) of  $\text{Zn}(\text{NO}_3)_2 \cdot 6\text{H}_2\text{O}$  and 0.1 g (1.3 mmol) of thioacetamide were dissolved in the above solution. The solution was then transferred to a 100 mL Teflon-lined autoclave and heated to 160 °C for 12 h. After cooling to room

temperature, the gray product was collected using centrifugation and further washed several times using ethanol and deionized water, and then dried at 60 °C for 18 h. Finally, the CNTs@ZnS was obtained by annealing the gray precursor under Ar atmosphere at 500 °C for 2 h.

**Synthesis of S/CNTs@ZnS.** A mixture of CNTs@ZnS and sulfur (70%, weigh ratio) was sealed in a glass bottle, and heated at 155 °C for 24 h in an oven. The S/CNTs was prepared using the same method without ZnS coating.

## 2.2 Structural characterizations

The phases and chemical compositions of all the products were analyzed by X-ray diffraction (XRD, D/max-RB, Rigaku with Cu  $\text{K}\alpha$  radiation). The morphology of the samples was performed using a scanning electron microscopy (SEM, JSM-7800F), transmission electron microscopy (F200X-G2) and field emission scanning transmission electron microscope (STEM). The sulfur content was measured under a nitrogen atmosphere through thermal gravimetric analysis (TGA).  $\text{N}_2$  adsorption/desorption isothermals were characterized by a gas adsorption analyzer (ASAP-2020). The Brunauer–Emmett–Teller (BET) method was used to calculate the specific surface areas and the Quenched Solid Density Function Theory (QSDFT) was used to calculate the pore-size distribution. UV–visible spectra were obtained using a Microsolar 300 UV–Vis absorption spectroscopy. The chemical composition were measured by XPS measurements (ESCALAB250 X-ray photoelectron spectrometer).

## 2.3 Polysulfide adsorption test

A polysulfide electrolyte was prepared using excess sulfur chemically reacting with lithium metal in electrolyte to form saturated solution of polysulfides. Subsequently, 10 mg of CNTs@ZnS and CNTs were respectively immersed into 1 mL of polysulfides saturated solution and electrolyte ( $v/v=9:1$ ). After resting for 12 h, the digital photos were taken to display the discoloration of the above samples and the adsorption precipitated product of CNTs@ZnS-LiPSs was studied using X-ray photoelectron spectroscopy.

## 2.4 Electrochemical measurements

The working cathodes were prepared by mixing 10% carbon black (Super P), 10% poly(vinylidene fluoride) binder (PVDF) and 80% active materials in N-methyl-pyrrolidone (NMP), followed by casting the slurry onto carbon paper and drying at 60 °C for 12 h in a vacuum oven. Finally, the slurry cathode was cut into discs with a diameter of 12 mm. The electrolyte/sulfur ratio was about 20  $\mu\text{L mg}^{-1}$  for cathodes. The 2032-type coin cells were assembled using

lithium foil as the anode and Celgard 2325 as membranes. The electrolyte used was a freshly prepared solution of lithium bis(trifluoromethanesulfonyl) imide. Electrochemical impedance spectroscopy (EIS) measurements and cyclic voltammetry (CV) were performed on an electrochemical workstation (CHI660E, Shanghai, China). CV curves were performed with a scan rate of 0.1  $\text{mV s}^{-1}$  between 1.8 and 3.0 V. Electrochemical Impedance Spectroscopy was tested in the frequency range between 0.01 Hz and 1000 kHz at an open circuit voltage of each cell. And galvanostatic cycling was carried out from 1.8 to 2.8 V using a battery measurement system (Neware, China).

## 2.5 Symmetrical cell assembly and electrochemical test

The symmetrical cells are designed by sandwiching lithium bis(trifluoromethanesulfonyl)imide (LiTFSI) electrolyte containing 0.5 M LiPSs between two identical CNTs@ZnS or CNTs electrodes as both the working and counter electrodes. The active materials and polyvinylidene difluoride (PVDF) binder (4:1, ratio by weight) were mixed in N-Methyl pyrrolidone (NMP). The electrode foil was punched to disks with a diameter of 12.0 mm and areal sulfur loading of 1–1.5  $\text{mg cm}^{-2}$ . The coin cells were assembled with two same disks as the cathode and anode, Celgard 2400 separator, and 40  $\mu\text{L}$  catholyte containing 0.5 M LiTFSI and 0.5 M LiPSs in DME/DOL ( $v/v=1/1$ ). CV measurements were obtained from a symmetric cell using a scanning rate of 3  $\text{mV s}^{-1}$  with potential window between –1.5 and 1.5 V.

## 3 Results and discussion

Figure 1a shows a schematic illustration of the preparation procedures of the S/CNTs@ZnS composite. As observed in scanning electron microscope (SEM) image in Fig. 1b, the carbon nanotubes (CNTs) obtained by the direct carbonization of polypyrrole-NTs shows a length of 3–5  $\mu\text{m}$  and a diameter of 100–150 nm with smooth surface. These CNTs are mixed with zinc nitrate and thioacetamide solution, followed hydrothermal treatment at 160 °C for 12 h. Subsequently calcining is carried out at 500 °C for 2 h in argon gas to obtain ZnS nanoparticles coated on CNTs (CNTs@ZnS). As shown in Fig. 1c, the as-formed CNTs@ZnS maintains the nanotube morphology of CNTs with small ZnS nanoparticles coated on CNTs. The thickness of outer layer is ~50–80 nm thickness, which can be clearly seen in TEM image (Fig. 2a). Meanwhile a certain mass of sulfur is homogeneously loaded on the CNTs@ZnS via physical deposition at 155 °C for 12 h to fabricate the aimed S/CNTs@ZnS. After sulfur loading, the morphology of S/



**Fig. 1** **a** Schematic illustration of the fabrication processes of S/CNTs@ZnS. **b–d** SEM images of **b** carbon nanotubes, **c** CNTs@ZnS and **d** S/CNTs@ZnS

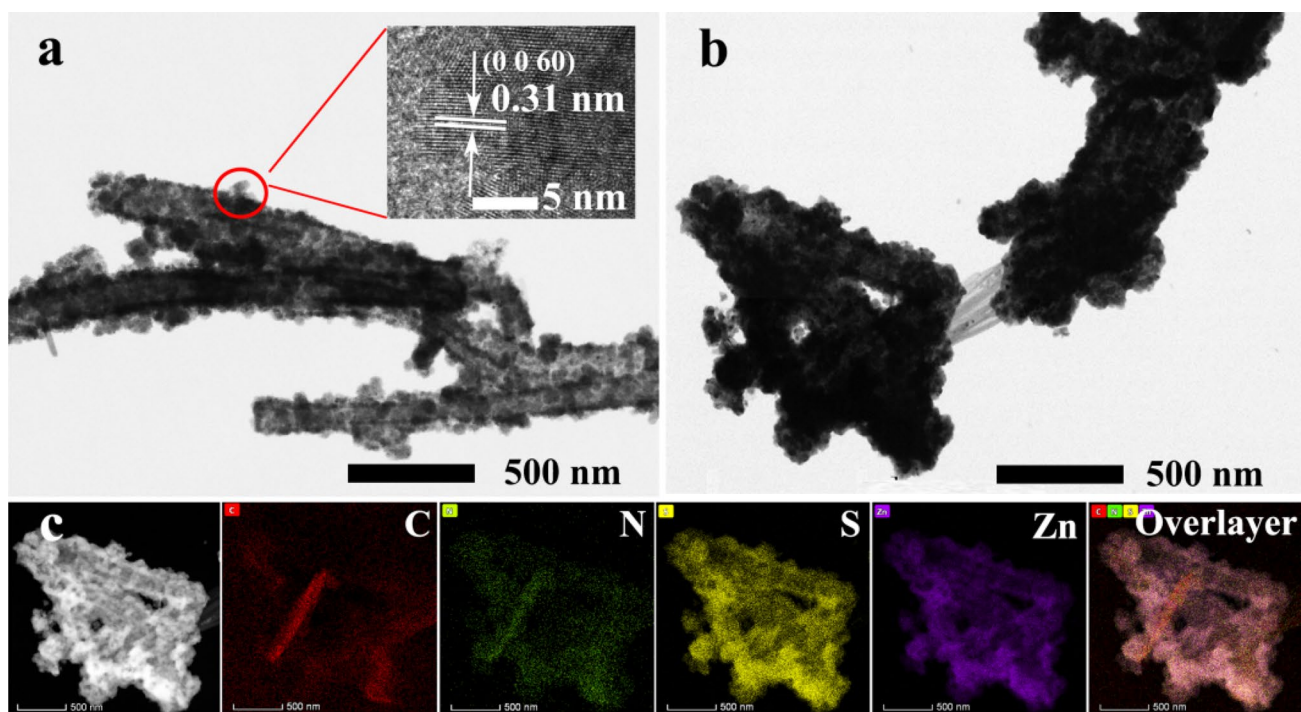
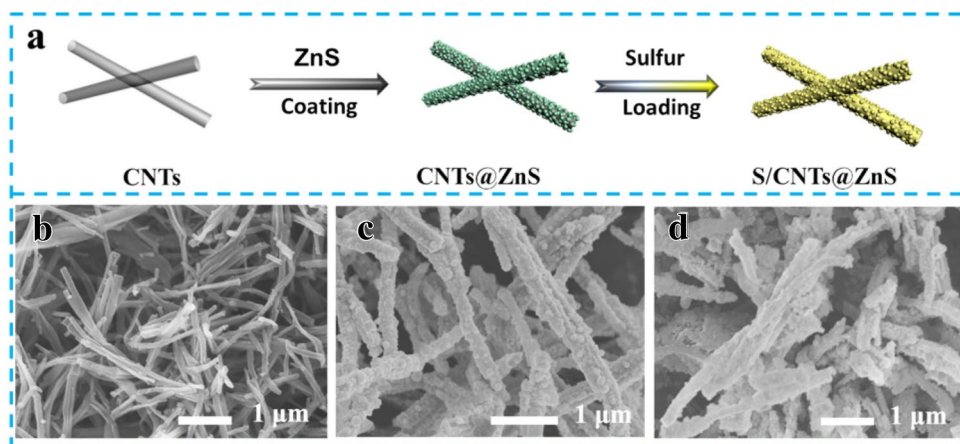


**Fig. 2** **a** TEM image of CNTs@ZnS (inset: HRTEM image). **b** TEM image of S/CNTs@ZnS. **c** STEM image of S/CNTs@ZnS and corresponding element maps of C, N, S and Zn. Scale bars, 500 nm

CNTs@ZnS is shown in Fig. 1d. The sulfur is distributed homogenous within CNTs@ZnS. And the sulfur content of S/CNTs@ZnS is measured to be 70 wt % (Figure S3). As confirmed by X-ray diffraction (XRD) pattern in Figure S1, only peaks attributable to ZnS (JCPDS 89-2173) are founded at 28.5°, 47.5° and 56.4°. For comparison, the ZnS nanospheres (Figure S2) obtained without CNTs get agglomerated. Correspondingly, in the XRD curve of S/CNTs@ZnS (Figure S1), orthorhombic sulfur (JCPDS 08-0247) related peaks are observed.

The N<sub>2</sub> adsorption/desorption profiles of CNTs@ZnS and CNTs are presented in Figure S4. Compared with CNTs (64.0

m<sup>2</sup> g<sup>-1</sup>), the low specific surface area of CNTs@ZnS (41.4 m<sup>2</sup> g<sup>-1</sup>) is ascribed to the existence of ZnS on the surface. To further investigate the structure and the elemental distribution of synthesized samples, the transmission electron microscope (TEM) images are further analyzed. As shown in Fig. 2a, a tubular structure with a diameter of 150–200 nm is clearly observed. This is in consistent with the SEM analysis. ZnS nanoparticles are founded to be interconnected along with 1D porous carbon nanotubes. In the high resolution transmission electron microscope (HRTEM) image (Fig. 2a, inset), a lattice fringe with space of 0.31 nm can be clearly observed, and is indexed to the (0 0 60)

plane of trigonal phase ZnS. The corresponding element mappings of CNTs@ZnS is shown in Figure S5. After loading sulfur, the TEM image of S/CNTs@ZnS in Fig. 2b reveals that the overall morphology is still retained. The HAADF image and the corresponding energy-dispersive X-ray spectroscopy (EDS) mappings of S/CNTs@ZnS is depicted in Fig. 2c. It suggests that the sulfur is either in ZnS or in the form of the sulfur deposited in the post loading step. Furthermore it is clear that the sulfur content is uniform on the CNTs.

In order to further probe the strong polysulfide capture capability of CNTs@ZnS, the visual test and ultraviolet/visible absorption spectra are carried out in Fig. 3a. This is done by dispersing 10 mg of CNTs@ZnS or CNTs powder in the polysulfide-saturated solution. Without the chemical capture capability between LiPSs and the polar cathode material, a large amount of intermediate polysulfide can easily diffuse away from the carbon cathode, resulting in serious shuttle effect and deposition of insoluble  $\text{Li}_2\text{S}_x$  ( $x \leq 2$ ). The adsorption ability of CNTs@ZnS composite can be shown by the color change of the typical polysulfides solution. As shown in Fig. 3a (inset), after 12 h aging, the polysulfides are effectively adsorbed by the immersing CNTs@ZnS; this correlates with change in color of corresponding solution (becomes nearly transparent). In contrast, the color of the polysulfides solution with CNTs

shows no obvious color fading. And it can be observed that there are two obvious absorption peaks of pristine LiPSs solution in the range at around 450 nm and 330 nm. The two peaks can be attributed to the absorbance peak of  $\text{Li}_2\text{S}_6/\text{Li}_2\text{S}_4$  and  $\text{Li}_2\text{S}_8/\text{Li}_2\text{S}_6$  [31]. The UV-Vis spectrum shows the absorbance for the solution of CNTs@ZnS after adsorption is nearly absent at 420 nm, confirming that the  $\text{Li}_2\text{S}_6/\text{Li}_2\text{S}_4$  species are absorbed by the CNTs@ZnS composite. The result indicates the strong chemical adsorption ability of CNTs@ZnS.

The X-ray photoelectron spectrum of CNTs@ZnS and CNTs@ZnS-LiPSs are further performed to provide proof for the strong chemical adsorption of LiPSs. The fine Li 1s spectrum of CNTs@ZnS (Fig. 3b) corresponds to a peak at 55.9 eV in addition to Li-S bond after adsorption of LiPSs. This in fact results in a 0.6 eV slightly shift to lower binding energy compared to the pristine  $\text{Li}_2\text{S}_6$  (56.3 eV) as literature reported [8]. The shift in the peak indicates the fast electron transfer from ZnS to lithium ion in the polysulfide solution. Also as shown in Fig. 3c, Zn 2p<sub>3/2</sub> peak of the CNTs@ZnS after loading of LiPSs is located at 1021.6 eV; which shifts to lower binding energy compared to that of CNTs@ZnS (1022.2 eV). It means that there exists a chemical reaction occurring between ZnS and LiPSs, which results in strong chemical bonds for LiPSs confinement. The Li 1s and Zn 2p<sub>3/2</sub> peaks indicate electron transfer

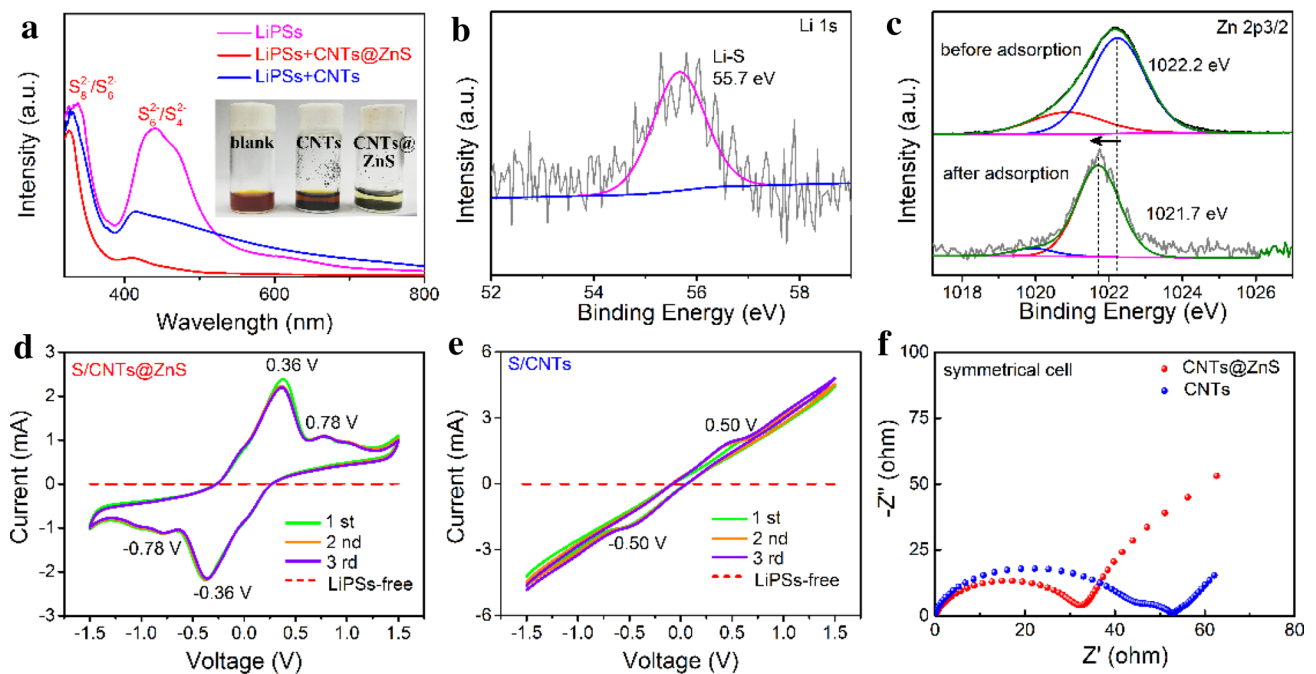


**Fig. 3** **a** UV-Vis spectra of LiPSs solution and upper solution after adsorption of the CNTs@ZnS and CNTs. The inset is photo of LiPSs adsorption performance after addition of CNTs and CNTs@ZnS. **b** XPS spectrum of Li 1s for CNTs@ZnS after adsorbing LiPSs. **c** XPS spectrum of Zn 2p<sub>3/2</sub> for CNTs@ZnS before and after adsorption

of LiPSs. CV curves of LiPSs and LiPSs-free symmetrical cell with **d** CNTs@ZnS and **e** CNTs working electrode with 1.2 mg cm<sup>-2</sup> sulfur loading each disk at a scan rate of 3 mV s<sup>-1</sup>. **f** EIS of the LiPSs symmetrical cell with CNTs@ZnS and CNTs cathodes

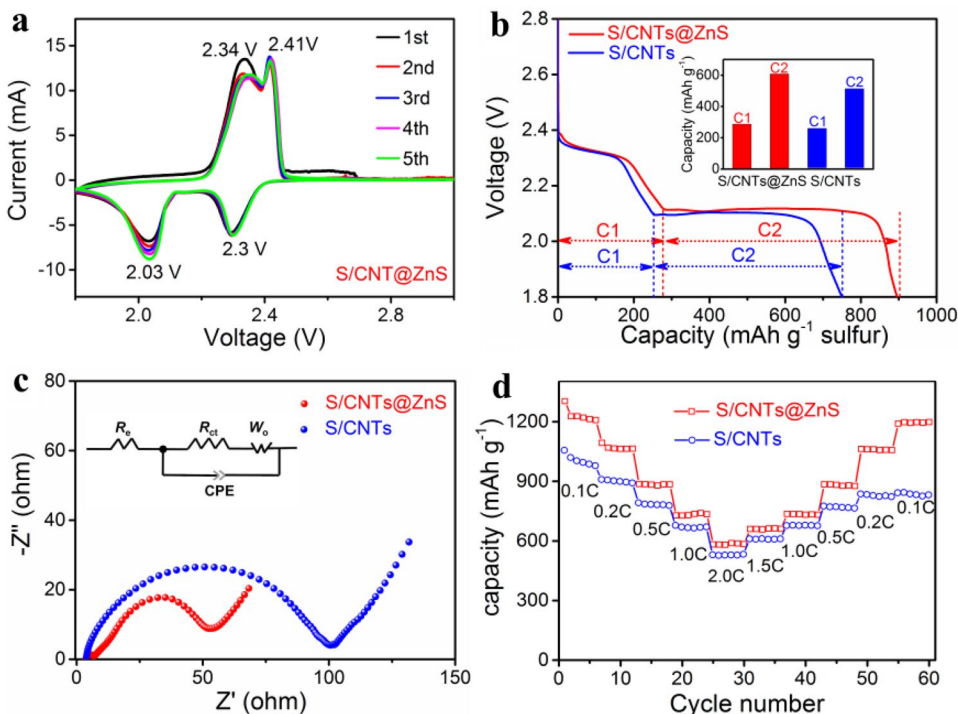
from LiPSs to the Zn atoms; which in turn, results in strong chemical adsorption.

To further probe the catalytic activity of CNTs@ZnS to LiPSs conversion in Li-S battery, symmetrical cells are designed for cyclic voltametric test in the voltage range - 1.5 to 1.5 V. The tests are done using an 3 mV s<sup>-1</sup> scanning rate for LiPSs and LiPSs-free symmetrical cells [32]. As shown in Fig. 3d-e, the CV curve of the LiPSs-free one (red dotted lines) shows a minor contribution to the current. With the addition of LiPSs into the counter electrodes, the symmetrical cells show a much higher current intensity, which means that the chemical reactions of lithiation with CNTs@ZnS devote the current response. And four peaks are observed at -0.78, -0.36, 0.36 and 0.78 V respectively. The LiPSs symmetrical cell with the CNTs@ZnS electrode shows facile polysulfide conversion and high reversibility in the first three cycles, which is much better than the LiPSs symmetrical cell with the CNTs (Fig. 3e). This clearly demonstrates the key role of ZnS in accelerating the electrochemical reactions with LiPSs. Meanwhile, the current density of CNTs@ZnS symmetrical cell is also higher than that of LiPSs symmetrical cell with ZnS electrode (Figure S6); this is a robust indicator of the role of carbon nanotubes in enhancing the conductivity. The electrochemical impedance spectroscopy (EIS) spectrum of the CNTs@ZnS and CNTs electrodes symmetrical cell are presented in Fig. 3f. The charge transfer resistance (R<sub>ct</sub>) on the CNTs@ZnS polysulfide interface is faster than that on the CNTs-polysulfide interface. Considering that the symmetric cells are free of lithium foil, the faster charge transfer can be

ascribed to the interfacial affinity between CNTs@ZnS and LiPSs and rapid charge transfer in the redox reaction of polysulfide conversion. This is also consistent with the CV results.

The electrochemical performance of S/CNTs@ZnS cathode is measured using the CR2032 cells with a lithium foil as the anode and DOL/DME (1:1, v/v) with 1 M LiTFSI and 2% LiNO<sub>3</sub> as the electrolyte. The S/CNTs and S/ZnS electrodes with same sulfur loading (1.2–1.3 mg cm<sup>-2</sup>) as S/CNTs@ZnS is used as the experimental control. Figure 4a presents the CV curves of the S/CNTs@ZnS electrode for the first five cycles in the 1.8–3.0 V at a scan rate of 0.1 mV s<sup>-1</sup>. The CV curves show two well-defined cathodic peaks at 2.3 and 2.03 V; this is ascribed to the redox reaction of sulfur to long-chain lithium polysulfide Li<sub>2</sub>S<sub>x</sub> (4 ≤ x ≤ 8) and consecutive conversion of Li<sub>2</sub>S<sub>x</sub> to short-chain sulfides (Li<sub>2</sub>S<sub>2</sub>/Li<sub>2</sub>S), respectively [33]. In the anodic sweep, the oxidation peaks at 2.34 and 2.41 V correspond to the oxidation of Li<sub>2</sub>S/Li<sub>2</sub>S<sub>2</sub> to long-chain polysulfides and ultimately to sulfur. For the initial five cycles, the peaks have no obvious shifts, indicating good electrochemical stability. Meanwhile compared with S/CNTs and S/ZnS (Figure S7), the S/CNTs@ZnS exhibits higher cathodic peaks potential, smaller anodic peaks and larger peaks currents. It suggests that the composite of CNTs@ZnS kinetically accelerates polysulfides redox conversion in some degree and is good for the fast transfer of electrons. Figure 4b compares the discharge curves of the S/CNTs@ZnS and S/CNTs electrodes at 0.5C (1C = 1673 mA h g<sup>-1</sup>). The S/CNTs@ZnS composite exhibits much higher initial

**Fig. 4** Electrochemical performance of S/CNTs@ZnS and S/CNTs. **a** CV curve of Li-S battery based on the S/CNTs@ZnS and S/CNTs cathode with above 1.2 mg cm<sup>-2</sup> sulfur loading at the scanning rate of 0.1 mV s; **b** Typical voltage profile of S/CNTs@ZnS and S/CNTs at 0.5C and the corresponding discharge capacity in stage 1 and 2 for S/CNTs@ZnS and S/CNTs are shown in inset image; **c** Electrochemical impedance spectra of S/CNTs@ZnS and S/CNTs at the open circuit voltage (inset: the equivalent circuits); **d** Rate performance at different C-rates of S/CNTs@ZnS and S/CNTs





discharge capacities of  $897 \text{ mAh g}^{-1}$  in comparison with S/CNTs composite ( $751 \text{ mAh g}^{-1}$ ), with initial Coulombic efficiency of 98.6%. C1 and C2 are the discharge capacities of two typical plateaus corresponding to the conversion of sulfur to soluble polysulfides and further reduction to insoluble  $\text{Li}_2\text{S}$ . Moreover, the capacity ratio (C2/C1) of S/CNTs@ZnS indicates improved polysulfide redox kinetics and higher sulfur utilization when compared with S/CNTs [34], which agrees with the results of CV curves of the symmetrical cells and lithium sulfur cell. The enhanced redox kinetics of S/CNTs@ZnS can be attributed to the synergistic effects of ZnS and CNTs. It provides higher electric conductivity for fast charge transfer of  $\text{Li}^+/\text{e}^-$  and also offers effective chemical adsorption of polysulfides for the conversion to  $\text{Li}_2\text{S}_2/\text{Li}_2\text{S}$  [35].

The EIS analysis and the corresponding equivalent circuit of the S/CNTs@ZnS, S/CNTs and S/ZnS electrodes after 10 cycles are displayed in Fig. 4c and Figure S8. As we all know, the start point of EIS spectra is the electrolyte resistance ( $R_e$ ) and the semicircle represents the charge transfer resistance ( $R_{ct}$ ) and relative capacitance (CPE). The sloped line in low frequency range corresponds to the Warburg impedance ( $W_o$ ), related to the diffusion of lithium ion in the electrode [36, 37]. A smaller charge transfer resistance ( $49.8 \Omega$ ) on the S/CNTs@ZnS electrode when compared to S/CNTs ( $97.0 \Omega$ ) and S/ZnS ( $144.8 \Omega$ ) indicates that the internal resistance of the Li-S battery system is reduced by the interaction of ZnS and CNTs. The results are consistent with CV results.

The lower resistance of charge transfer implies faster charge transfer rate due to the enhanced interfacial affinity and faster redox kinetics on the S/CNTs@ZnS electrode [23, 38]. Figure 4d shows the rate capability of the S/CNTs@ZnS and S/CNTs cathode electrodes at various rates from 0.1 to 2C. With the current increase, the capacity decreases, and the S/CNTs@ZnS cathode has larger capacities and rate capability than that of S/CNTs cathode at all rates. Especially, when the current returns to 0.1 C after 54 cycles, the capacity ( $1181 \text{ mA h g}^{-1}$ ) of S/CNTs@ZnS cathode shows no abrupt degradation; this is much better than S/CNTs ( $838 \text{ mA h g}^{-1}$ ), indicating high electrochemical reversibility.

The long term cycling performance of S/CNTs@ZnS is shown in Fig. 5. Figure 5a and Figure S9 show the cycling performance and Coulombic efficiency of the S/CNTs@ZnS and S/CNTs cathodes at 0.2C and 1C ( $1 \text{ C} = 1672 \text{ mAh g}^{-1}$ ). It can be observed that the existence of ZnS nanoparticles alleviates the polysulfide shuttle effect with  $1.51 \text{ mg cm}^{-2}$  areal sulfur loading. As shown in Fig. 5a, S/CNTs@ZnS cathode yields an initial capacity of  $1069 \text{ mA h g}^{-1}$ . Furthermore, it retains a high reversible capacity of  $1003 \text{ mA h g}^{-1}$  after 100 cycles at 0.2 C with Coulombic efficiency close to 100%. In contrast, the initial capacity

of S/CNTs is  $905 \text{ mA h g}^{-1}$  and after 100 cycles the capacity ( $813 \text{ mAh g}^{-1}$ ), which is lower than S/CNTs@ZnS. S/ZnS cathode was also prepared to assess the structural advantage of CNTs@ZnS. As shown in Figure S10, the S/ZnS electrodes exhibit a low initial specific capacity of  $1055 \text{ mAh g}^{-1}$  at 0.2C and the capacity quickly drops to  $717 \text{ mAh g}^{-1}$  after 100 cycles, suggesting the low sulfur utilization than S/CNTs@ZnS. Meanwhile, the S/CNTs@ZnS cathode exhibits slower capacity decay (0.06% per cycle) than S/CNTs (0.1% per cycle) and S/ZnS (0.3% per cycle), which shows an obvious improvement in the cycling performance due to the synergistic effect of CNTs and ZnS. The cycling performances of S/CNTs@ZnS with  $1.27 \text{ mg cm}^{-2}$  sulfur loading and S/CNTs with  $1.3 \text{ mg cm}^{-2}$  sulfur loading at 1C are also shown in Fig. 5a and S9 respectively. The reversible discharge capacity for S/CNTs@ZnS is  $719 \text{ mAh g}^{-1}$  after 100 cycles, higher than the S/CNTs electrode. To understand the stabilities of S/CNTs@ZnS electrode, the prolonged cycling performance is evaluated at 0.5C. As shown in Fig. 5b, S/CNTs@ZnS electrode delivers an initial capacity of  $843 \text{ mAh g}^{-1}$  after activation at 0.1C. After 500 cycles at 0.5C, S/CNTs@ZnS electrode still retains a relative high discharge capacity of  $655 \text{ mAh g}^{-1}$ . The capacity retention is calculated to be 77.6% corresponding to a capacity decay of 0.04% per cycle. Meanwhile, the prolonged cycling stability of S/CNTs@ZnS at 0.5C for 1000 cycles is presented in Figure S11. During the whole cycling, the Coulombic efficiency is higher than 95%. We further measured the S/CNTs@ZnS with high sulfur loading of  $3.1 \text{ mg cm}^{-2}$ ; the cathode shows a high discharge capacity of  $670 \text{ mAh g}^{-1}$  at 0.2C and the capacity retention is 0.05% per cycle after 500 cycles (Fig. 5c). These results confirm that S/CNTs@ZnS delivers outstanding electrochemical performance because of the chemical adsorption and catalytic capability of the polar ZnS to LiPSs and the improved conductivity of the CNTs@ZnS.

Finally, according to the above results and analyses, the polysulfide adsorption and conversion process on the surface of the CNTs@ZnS during discharge-charge can be illustrated schematically in Fig. 6. The polar host material of ZnS can restrain the shuttle effect of polysulfides by effective chemical adsorption. Also, the short chain sulfur species can rapidly result in redox on the CNTs@ZnS surface during the reaction processes due to the high electrical conductivity of CNTs and excellent chemical reaction activity of ZnS. Meanwhile, the enhanced electrochemical performance of S/CNTs@ZnS can be attributed to the synergistic effect associated with both ZnS and CNTs. It provides higher electric conductivity for fast charge transfer of  $\text{Li}^+/\text{e}^-$  and effective

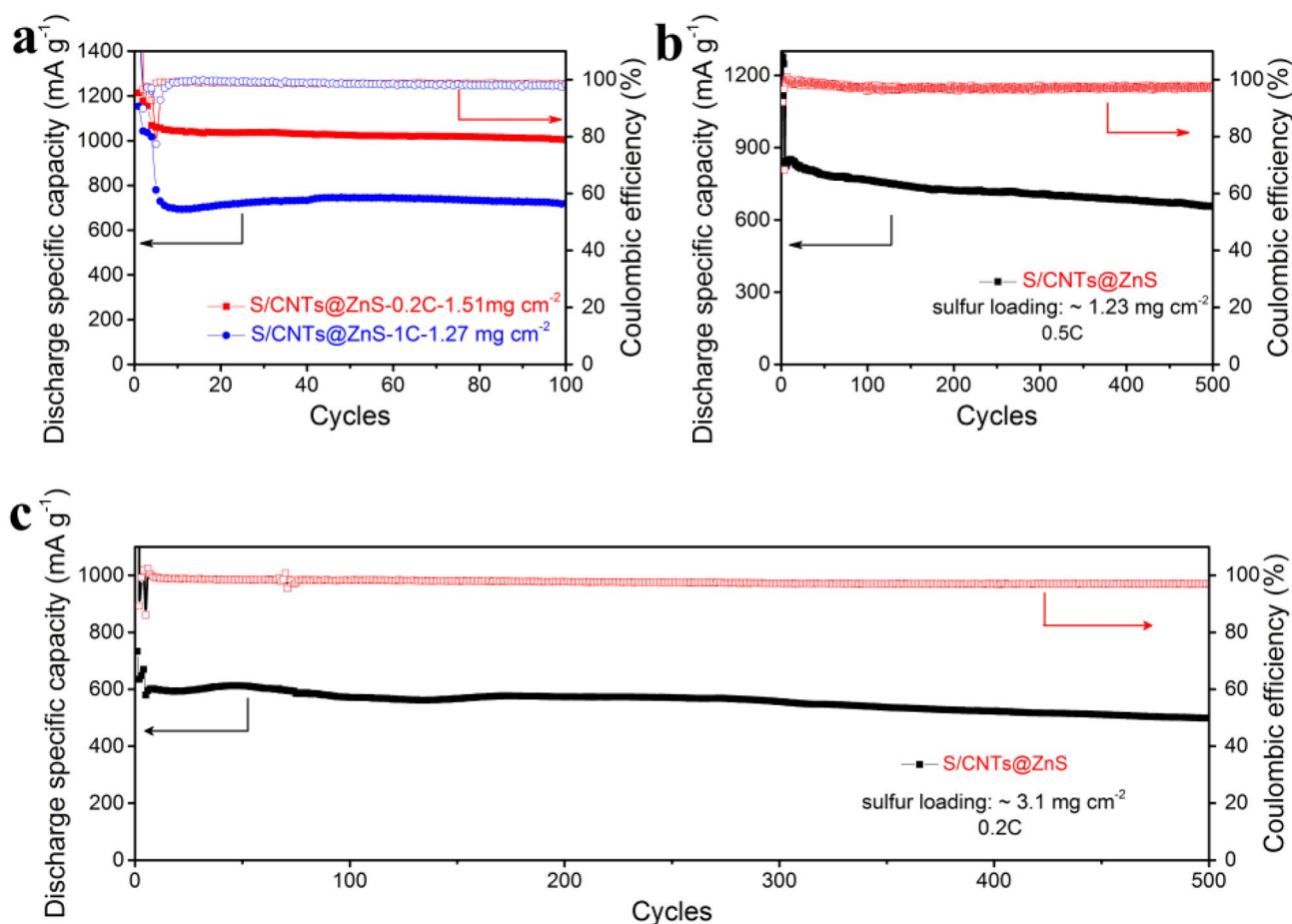


**Fig. 5** Long term cycling ability of S/CNTs@ZnS. **a** Cycling stability at 0.2C and 1C of S/CNTs@ZnS; **b** Cycling ability at 0.5C of S/CNTs@ZnS; **c** Long term cycling ability of S/CNTs@ZnS at 0.2C with high sulfur loading of  $3.1 \text{ mg cm}^{-2}$  for 500 cycles

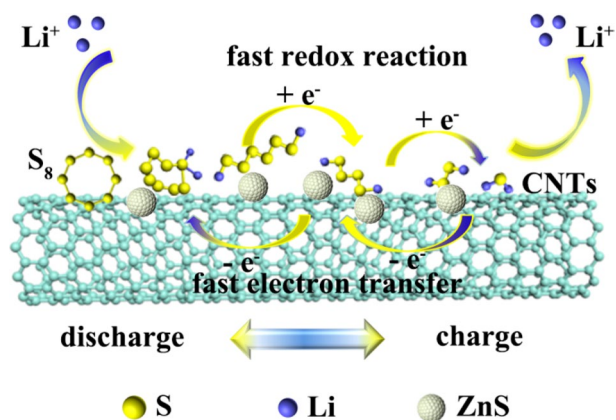


**Fig. 6** Illustration of the enhanced redox reaction of the polysulfide using the catalyzing effect of CNTs@ZnS during charge–discharge

chemical adsorption of polysulfides for the conversion to  $\text{Li}_2\text{S}_2/\text{Li}_2\text{S}$ .

## 4 Conclusions

In summary, CNTs@ZnS composites are designed and synthesized as a host cathode material for lithium sulfur batteries using a facile wet chemical method. The host suppresses the polysulfide’s shuttle effect and further enhances the observed activity. The host materials unique structure provides high conductivity for charge transfer. It also offers sufficient chemical adsorption sites to anchor the LiPSs on to the reactive interfaces of ZnS. This in fact is responsible for the observed alleviation of the shuttle effect.

XPS reveals that the CNTs@ZnS interacts with LiPSs through the formation Li–S bonds and ZnS–S bonds. These bonds catalytically accelerate the conversion of soluble polysulfides into insoluble  $\text{Li}_2\text{S}$ . The CNTs@ZnS cathode delivers a stable specific capacity with  $3.1 \text{ mg cm}^{-2}$  sulfur loading after 500 cycles at 0.2C and ultra-long cycling performance at 0.5C with 0.04% capacitance decay per cycle. The strategy described in this



work provides a novel route for improving the electrochemical performance of lithium sulfur batteries.

**Acknowledgements** This work is supported by Key Program of the Chinese Academy of Sciences (KFZD-SW-320), China Postdoctoral Science Foundation (2019M652155) and Opened Fund of the State Key Laboratory on Integrated Optoelectronics (IOSKL2017KF08M). M. Yang appreciates the support from the Ningbo 3315 program. J. Wang would like to thank the financial support from the Science & Technology Innovation Major Program of Ningbo (Ningbo 2025 Program, 2018B10056). Tiju Thomas is thankful to DST India for support via DST FILE NO. DST/TMD/SERI/HUB/1(C), and Materials for Energy Storage project.

## Compliance with ethical standards

**Conflict of interest** There are no conflicts to declare.

## References

- Evers S, Nazar LF (2013) New approaches for high energy density lithium-sulfur battery cathodes. *Acc Chem Res* 46(5):1135–1143
- Liu Y-T, Han D-D, Wang L, Li G-R, Liu S, Gao X-P (2019) NiCo<sub>2</sub>O<sub>4</sub> Nanofibers as carbon-free sulfur immobilizer to fabricate sulfur-based composite with high volumetric capacity for lithium-sulfur battery. *Adv Energy Mater* 9(11):1803477
- Liu S, Li Y, Zhang C, Chen X, Wang Z, Cui F, Yang X, Yue W (2020) Amorphous TiO<sub>2</sub> nanofilm interface coating on mesoporous carbon as efficient sulfur host for lithium-sulfur batteries. *Electrochim Acta* 332:135458
- Zhang H, Hu X, Zhang Y, Wang S, Xin F, Chen X, Yu D (2018) 3D-crosslinked tannic acid/poly(ethylene oxide) complex as a three-in-one multifunctional binder for high-sulfur-loading and high-stability cathodes in lithium-sulfur batteries. *Energy Storage Mater* 17:293–299
- Ding G, Li Y, Zhang Y, Huang C, Yao X, Lin K, Shen K, Yan W, Sun F, Zhou L (2019) Waste to Wealth: exhausted Nitrogen-Doped Mesoporous Carbon/MgO Desulfurizers Turned to High-Sulfur-Loading Composite Cathodes for Li-S Batteries. *ACS Appl Mater Inter* 11(21):19096–19103
- Peled E, Sternberg Y, Gorenshtein A, Lavi Y (1989) Lithium-sulfur battery: evaluation of dioxolane-based electrolytes. *J Electro Soc* 136:1621–1625
- Manthiram A, Fu Y, Su Y-S (2013) Challenges and prospects of lithium-sulfur batteries. *Acc Chem Res* 46(5):1125–1134
- Song X, Chen G, Wang S, Huang Y et al (2018) Self-assembled close-packed MnO<sub>2</sub> nanoparticles anchored on a polyethylene separator for lithium-sulfur batteries. *ACS Appl Mater Inter* 10(31):26274–26282
- Chen M, Zheng J, Sheng O, Jin C, Yuan H, Liu T, Liu Y, Wang Y, Nai J, Tao X (2019) Sulfur-Nitrogen co-doped porous carbon nanosheets to control the lithium growth for stable lithium metal anode. *J Mater Chem A* 7(31):18267–18274
- Pope MA, Aksay IA (2015) Structural design of cathodes for Li-s batteries. *Adv Energy Mater* 5(16):1500124
- Wang JL, Yang J, Wan CR, Du K, Xie JY, Xu NX (2003) Sulfur composite cathode materials for rechargeable lithium batteries. *Adv Funct Mater* 13(6):487–492
- Pang Q, Liang X, Kwok CY, Nazar LF (2016) Advances in lithium-sulfur batteries based on multifunctional cathodes and electrolytes. *Nat Energy* 1(9):16132
- Deng D-R, Xue F, Jia Y-J, Ye J-C, Bai C-D, Zheng M-S, Dong Q-F (2017) Co<sub>4</sub>N nanosheet assembled mesoporous sphere as a matrix for ultrahigh sulfur content lithium-sulfur batteries. *ACS Nano* 11(6):6031–6039
- Ansari Y, Zhang S, Wen B, Fan F, Chiang Y-M (2019) Stabilizing Li-S battery through multilayer encapsulation of sulfur. *Adv Energy Mater* 9(1):1802213
- Xiao Z, Yang Z, Wang L, Nie H, Zhong M, Lai Q, Xu X, Zhang L, Huang S (2015) A lightweight TiO<sub>2</sub>/Graphene interlayer, applied as a highly effective polysulfide absorbent for fast Long-Life Lithium-Sulfur batteries. *Adv Mater* 27(18):2891–2898
- Lang S-Y, Shi Y, Guo Y-G, Wang D, Wen R, Wan L-J (2016) Insight into the interfacial process and mechanism in lithium-sulfur batteries: an in situ AFM study. *Angew Chem Inter Edition* 55(51):15835–15839
- Wei H, Rodriguez EF, Best AS, Hollenkamp AF, Chen D, Caruso RA (2017) Chemical bonding and physical trapping of sulfur in mesoporous magnéli Ti<sub>4</sub>O<sub>7</sub> microspheres for high-performance li-s battery. *Adv Energy Mater* 7(4):1601616
- Luo L, Manthiram A (2017) Rational design of high-loading sulfur cathodes with a poached-egg-shaped architecture for long-cycle lithium-sulfur batteries. *ACS Energy Lett* 2(10):2205–2211
- Li Z, Huang Y, Yuan L, Hao Z, Huang YJC (2015) Status and prospects in sulfur-carbon composites as cathode materials for rechargeable lithium-sulfur batteries. 92:41–63
- Xu J, Lawson T, Fan H, Su D, Wang G (2018) Updated metal compounds (MOFs, -S, -OH, -N, -C) used as cathode materials for lithium-sulfur batteries. *Adv Energy Mater* 8(10):1702607
- Yao Y, Zeng L, Hu S, Jiang Y, Yuan B, Yu Y (2017) Binding S<sub>0.6</sub>Se<sub>0.4</sub> in 1D carbon nanofiber with C-S bonding for high-performance flexible Li-S batteries and Na-S batteries. *Small* 13(19):1603513
- Hu G, Xu C, Sun Z et al (2016) 3D graphene-foam-reduced-graphene-oxide hybrid nested hierarchical networks for high-performance Li-s batteries. *Adv Mater* 28(8):1603–1609
- Wu X, Du Y, Wang P, Fan L, Cheng J, Wang M, Qiu Y, Guan B, Wu H, Zhang N, Sun K (2017) Kinetics enhancement of lithium-sulfur batteries by interlinked hollow MoO<sub>2</sub> sphere/nitrogen-doped graphene composite. *J Mater Chem A* 5(48):25187–25192
- Chen A, Liu W, Hu H, Chen T, Ling B, Liu K (2018) Three-dimensional TiO<sub>2</sub>-B nanotubes/carbon nanotubes intertwined network as sulfur hosts for high performance lithium-sulfur batteries. *J Power Sources* 400:23–30
- Wei Seh Z, Li W, Cha JJ, Zheng G, Yang Y, McDowell MT, Hsu PC, Cui Y (2013) Sulphur-TiO<sub>2</sub> yolk-shell nanoarchitecture with internal void space for long-cycle lithium-sulphur batteries. *Nat Commun* 4:1331
- Li X, Lu Y, Hou Z, Zhang W, Zhu Y, Qian Y, Liang J, Qian Y (2016) SnS<sub>2</sub>- Compared to SnO<sub>2</sub>-Stabilized S/C Composites toward High-Performance Lithium Sulfur Batteries. *ACS Appl Mater Inter* 8(30):19550–19557
- Li Z, Zhang J, Lou XW (2015) Hollow carbon nanofibers filled with MnO<sub>2</sub> nanosheets as efficient sulfur hosts for lithium-sulfur batteries. *Angew Chem Inter Edition* 54(44):12886–12890
- Ni L, Wu Z, Zhao G, Sun C, Zhou C, Gong X, Diao G (2017) Core-shell structure and interaction mechanism of gamma-MnO<sub>2</sub> coated sulfur for improved lithium-sulfur batteries. *Small* 13(14):1603466
- Lin H, Zhang S, Zhang T, Cao S, Ye H, Yao Q, Zheng GW, Lee JY (2019) A cathode-integrated sulfur-deficient Co<sub>9</sub>S<sub>8</sub> catalytic interlayer for the reutilization of “lost” polysulfides in lithium-sulfur batteries. *ACS Nano* 13(6):7073–7082
- Jiang S, Chen M, Wang X, Wu Z, Zeng P, Huang C, Wang Y (2018) MoS<sub>2</sub>-coated N-doped mesoporous carbon spherical composite cathode and CNT/Chitosan modified separator for advanced lithium sulfur batteries. *ACS Sustain Chem Eng* 6(12):16828–16837

31. Fang R, Zhao S, Sun Z, Wang DW, Cheng HM, Li F (2017) More reliable lithium-sulfur batteries: status, solutions and prospects. *Adv Mater* 29(48):1606823
32. Huang SZ, Lim YV, Zhang XM, Wang Y, Zheng Y, Kong DZ, Ding M, Yang SYA, Yang HY (2018) Regulating the polysulfide redox conversion by iron phosphide nanocrystals for high-rate and ultrastable lithium-sulfur battery. *Nano Energy* 51:340–348
33. Li G, Sun J, Hou W, Jiang S, Huang Y, Geng J (2016) Three-dimensional porous carbon composites containing high sulfur nanoparticle content for high-performance lithium-sulfur batteries. *Nat Commun* 7:10601
34. Su D, Cortie M, Fan H, Wang G (2017) Prussian Blue Nanocubes with an Open Framework Structure Coated with PEDOT as High-Capacity Cathodes for Lithium-Sulfur Batteries. *Adv Mater* 29(48):1700587
35. Fu K, Gong Y, Hitz GT, McOwen DW et al (2017) Three-dimensional bilayer garnet solid electrolyte based high energy density lithium metal-sulfur batteries. *Energy Environ Sci* 10(7):1568–1575
36. Wang Y, Zhang R, Pang Y-c, Chen X et al (2019) Carbon@titanium nitride dual shell nanospheres as multi-functional hosts for lithium sulfur batteries. *Energy Storage Mater* 16:228–235
37. Wang C, Wan W, Chen J-T, Zhou H-H, Zhang X-X, Yuan L-X, Huang Y-H (2013) Dual core-shell structured sulfur cathode composite synthesized by a one-pot route for lithium sulfur batteries. *J Mater Chem A* 1(5):1716–1723
38. Yun JH, Kim J-H, Kim DK, Lee H-W (2018) Suppressing polysulfide dissolution via cohesive forces by interwoven carbon nanofibers for high-areal-capacity lithium-sulfur batteries. *Nano Lett* 18(1):475–481

**Publisher's Note** Springer Nature remains neutral with regard to jurisdictional claims in published maps and institutional affiliations.